

Linearized spectrum correlation analysis for line emission measurements

T. Nishizawa, M. D. Nornberg, D. J. Den Hartog, and J. S. Sarff

Citation: [Review of Scientific Instruments](#) **88**, 083513 (2017); doi: 10.1063/1.4999450

View online: <http://dx.doi.org/10.1063/1.4999450>

View Table of Contents: <http://aip.scitation.org/toc/rsi/88/8>

Published by the [American Institute of Physics](#)

Articles you may be interested in

[A high voltage pulse generator based on silicon-controlled rectifier for field-reversed configuration experiment](#)
Review of Scientific Instruments **88**, 083507 (2017); 10.1063/1.4997077

[Power measurements and coupler optimization in inductive discharges](#)
Review of Scientific Instruments **88**, 083512 (2017); 10.1063/1.4995810

[Correlation electron cyclotron emission diagnostic in TCV](#)
Review of Scientific Instruments **88**, 083506 (2017); 10.1063/1.4997075

[Gated ion spectrometer for spectroscopy of neutral particles](#)
Review of Scientific Instruments **88**, 083303 (2017); 10.1063/1.4997192

[A new high sensitivity far-infrared laser interferometer for the HL-2A tokamak](#)
Review of Scientific Instruments **88**, 083508 (2017); 10.1063/1.4997070

[The world's smallest capacitive dilatometer, for high-resolution thermal expansion and magnetostriction in high magnetic fields](#)
Review of Scientific Instruments **88**, 083903 (2017); 10.1063/1.4997073



Obstruction free access
optical table with integrated cryocooler



Various Objective Options

attoDRY800

- Cryogenic Temperatures
- Ultra-Low Vibration
- Optical Table Included
- Fast Cooldown



5% DISCOUNT
on all nanopositioners purchased
for your attoDRY800 set-up*
Coupon Code: PTJAD800

*valid for quotations issued before November, 2017

Linearized spectrum correlation analysis for line emission measurements

T. Nishizawa,^{a)} M. D. Nornberg, D. J. Den Hartog, and J. S. Sarff

Department of Physics, University of Wisconsin–Madison, Madison, Wisconsin 53706, USA

(Received 27 April 2017; accepted 7 August 2017; published online 22 August 2017)

A new spectral analysis method, Linearized Spectrum Correlation Analysis (LSCA), for charge exchange and passive ion Doppler spectroscopy is introduced to provide a means of measuring fast spectral line shape changes associated with ion-scale micro-instabilities. This analysis method is designed to resolve the fluctuations in the emission line shape from a stationary ion-scale wave. The method linearizes the fluctuations around a time-averaged line shape (e.g., Gaussian) and subdivides the spectral output channels into two sets to reduce contributions from uncorrelated fluctuations without averaging over the fast time dynamics. In principle, small fluctuations in the parameters used for a line shape model can be measured by evaluating the cross spectrum between different channel groupings to isolate a particular fluctuating quantity. High-frequency ion velocity measurements (100–200 kHz) were made by using this method. We also conducted simulations to compare LSCA with a moment analysis technique under a low photon count condition. Both experimental and synthetic measurements demonstrate the effectiveness of LSCA. *Published by AIP Publishing.* [<http://dx.doi.org/10.1063/1.4999450>]

I. INTRODUCTION

The transport of particles and heat due to plasma turbulence is a longstanding challenge for both experimental measurements and theoretical modeling. Measurements of micro-instabilities are especially challenging since they have a physical scale comparable to the gyro-radius and therefore tend to also be of high frequency. Much of the interesting volume in hot plasmas is inaccessible to probe-based diagnostics. This motivates measurements of micro-instabilities and their effect on ion dynamics using diagnostics such as CHARGE Exchange Recombination Spectroscopy (CHERS) and passive Ion Doppler Spectroscopy (IDS). A major limiting factor for time resolution in these techniques is the Poisson noise that arises from the discrete nature of photons. The relative uncertainty due to the Poisson noise scales as $(\int_t^{t+\Delta t} \Gamma dt')^{-1/2}$ in a photon detection system, where Γ and Δt are the incident photon flux and signal integration time, respectively. The Poisson noise can be reduced by increasing either Γ or Δt . Since Δt determines the time resolution, diagnosticians typically design high throughput spectrometers to optimize Γ . For example, at DIII-D, a spectrometer with a high light collection capability (étendue of 1.6 mm² sr and grating transmission efficiency of $\approx 75\%$ – 85%) and a dedicated light detection system are deployed for CHERS.^{1,2} This system can collect a sufficient number of photons to fit an emission line to measure ion dynamics with a time resolution of 1 μ s. The Ion-Doppler Spectrometer³ (IDS-II) at the Madison Symmetric Torus⁴ (MST) with an étendue of 0.80 mm²sr and transmission efficiency of 6% was also upgraded to measure high-frequency fluctuations (<400 kHz) and has successfully resolved 100 kHz C III emission fluctuations due to small scale

fluctuations.^{5–7} However, even with the use of diagnostic systems with a high light collection capability, the Poisson noise sets a noise floor in frequency power spectral density, which is problematic especially at high frequencies where signal amplitudes tend to be small.

In CHERS or IDS, ion dynamics are typically inferred from impurity line emission using Moment Analysis^{8,9} (MA) or line shape fitting.^{1,9–11} Moment analysis uses the zeroth moment for the emission intensity, the first moment for the line-of-sight velocity, and the second moment for the impurity ion temperature, e.g., $T_I \propto \sum I_j (\lambda_j - \lambda_0)^2 / \sum I_j$ where T_I , I_j , λ_j , and λ_0 are the impurity ion temperature, signal intensity, wavelength of channel j , and mean wavelength of the emission line, respectively. In MA, amplitudes of noise floors due to the Poisson noise can be estimated analytically. For example, the noise floor for the normalized intensity fluctuation power spectrum is

$$P_{f,\text{noise}} = \frac{1}{f_{\text{Nyquist}} \sum_j n_j}, \quad (1)$$

where f_{Nyquist} is the Nyquist frequency and n_j is the number of photons detected in the spectral channel, j . The noise levels for the velocity and temperature fluctuations are derived in Ref. 9. In line shape fitting, the noise levels can be reduced by adding a physics-based assumption such as a model for the emission line shape to find the most probable values for the fitting parameters.⁹ However, the Poisson noise still limits the resolution of line emission measurements. Even when the intensity fluctuations are resolved, the velocity or temperature fluctuation level can be much smaller than the noise level since the higher moments are more prone to noise accumulation.

In this paper, we describe a new linearized spectrum correlation analysis (LSCA) method that can isolate fast dynamics of the emission spectrum in low-light conditions and thereby

^{a)} nishizawa@wisc.edu

better expose the underlying plasma turbulence characteristics. The LSCA method is motivated by trying to detect the radial velocity fluctuations due to a stationary wave superimposed on a slowly evolving background in the C III impurity emission data in MST plasmas.⁵ Neither line shape fitting nor MA is able to resolve the fluctuations. The method's basis in correlation analysis allows greater noise rejection than that is possible for MA or line shape fitting, which converge to a certain noise floor even as the sample size increases. The advantage of correlation analysis has already been demonstrated in Correlation Electron Cyclotron Emission (CECE). By correlating two distinct radiometer signals, electron temperature fluctuations with amplitudes smaller than wave noise can be measured.^{12,13} In analogy with CECE, LSCA rejects the Poisson noise that is not correlated between the spectral channels. The LSCA procedure is outlined by the following steps:

1. Prepare an ensemble of time series with similar average plasma conditions.
2. Use line shape fitting to determine the average line shape.
3. Subdivide spectral channels into two sets and sum the signals in each set.
4. Calculate the cross spectrum of the two sets using efficient FFT methods.
5. Iterate the cross spectrum calculation using different sets of channels to isolate fluctuations in the parameters used for a line shape model.

The technique assumes small fluctuations that are identified by linearization around a line shape as discussed in Sec. II. We apply LSCA to experimental data in Sec. III which explains how to extract specific physical quantities by evaluating cross spectra. In Sec. IV, we compare LSCA and MA using synthesized data.

II. LINEARIZING THE SPECTROMETER OUTPUT

In CHERS or IDS, a spectral channel output $s_j(t)$ is the convolution of the spectral radiance $R(\lambda, t)$ and its instrumental transfer function $H_j(\lambda)$, where j is the spectral channel index. In line emission measurements, R can be written as follows:

$$R(\lambda, t) = I(t)G(\lambda, a_1(t), a_2(t), \dots, a_N(t)) + B(t), \quad (2)$$

where $I(t)$ is the intensity of the line emission, G is a normalized line shape parametrized by a_i , $i = 1, \dots, N$, and B is the background emission. While LSCA can be used to measure fluctuations in I and a_i for any given line shape, we restrict this paper to the case where R depends on the Doppler shift, $\lambda_d(t)$, and thermal broadening, $\sigma_{th}(t)$. This corresponds to a Maxwell-Boltzmann distribution, which is the most probable ion distribution in magnetized fusion plasmas.^{1,9-11}

After subtracting the background contribution, s_j is given by

$$s_j(t) = I(t) \int_{-\infty}^{+\infty} G(\lambda, \lambda_d(t), \sigma_{th}^2(t)) H_j(\lambda) d\lambda + X_j(t), \quad (3)$$

where X_j is a noise term.

When fluctuations are small, and s_j is a stationary random process over the time t , Eq. (3) can be linearized with respect to the quantities I , λ_d , and σ_{th}^2 around their time averages by the Taylor expansion,

$$\begin{aligned} s_j(t) \approx & I_0 \int_{-\infty}^{+\infty} G(\lambda, \lambda_{d,0}, \sigma_{th,0}^2) H_j(\lambda) d\lambda \\ & + \tilde{I}(t) \int_{-\infty}^{+\infty} G(\lambda, \lambda_{d,0}, \sigma_{th,0}^2) H_j(\lambda) d\lambda \\ & + \tilde{\lambda}_d(t) I_0 \int_{-\infty}^{+\infty} \frac{\partial G}{\partial \lambda_d}(\lambda, \lambda_{d,0}, \sigma_{th,0}^2) H_j(\lambda) d\lambda \\ & + \tilde{\sigma}_{th}^2(t) I_0 \int_{-\infty}^{+\infty} \frac{\partial G}{\partial \sigma_{th}^2}(\lambda, \lambda_{d,0}, \sigma_{th,0}^2) H_j(\lambda) d\lambda \\ & + X_j(t), \end{aligned} \quad (4)$$

where

$$\begin{aligned} I(t) &= I_0 + \tilde{I}(t), \\ \lambda_d(t) &= \lambda_{d,0} + \tilde{\lambda}_d(t), \\ \sigma_{th}^2(t) &= \sigma_{th,0}^2 + \tilde{\sigma}_{th}^2(t), \end{aligned} \quad (5)$$

and X_j represents the signal contribution from uncorrelated noise. See the Appendix for the details of the approximation assumptions. The magnitude of the coefficients for each fluctuating term is different for different j as shown in Fig. 1. When fluctuations are small, any change in the emission line shape can be represented through the superposition of these three patterns plus the noise term. It is important to note that, while a specific parameterization of the line shape defines the reference for linearization, LSCA is not a line-fitting algorithm. For the specific case here, any critical information in the underlying ion distribution that arises from being non-Gaussian is maintained in the data and ascribed to intensity, Doppler shift, and thermal broadening.

We introduce two disjoint sets of the available spectral channels, labeled A and B . We define $s_A(t)$ as the sum of signals

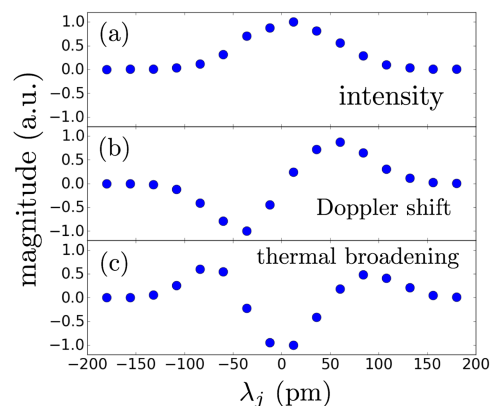


FIG. 1. Example of the linearized fluctuation patterns for the emission. The intensity (a), Doppler shift (b), and thermal broadening (c) correspond to the second, third, and fourth term on the right-hand side of Eq. (4). λ_j is the wavelength of spectral channel j with respect to the peak of the emission line.

in set A , i.e.,

$$\begin{aligned}
s_A(t) &\equiv I_0 \int_{-\infty}^{+\infty} G(\lambda, \lambda_{d,0}, \sigma_{th,0}^2) \sum_{j \in A} H_j(\lambda) d\lambda \\
&+ \tilde{I}(t) \int_{-\infty}^{+\infty} G(\lambda, \lambda_{d,0}, \sigma_{th,0}^2) \sum_{j \in A} H_j(\lambda) d\lambda \\
&+ \tilde{\lambda}_d(t) I_0 \int_{-\infty}^{+\infty} \frac{\partial G}{\partial \lambda_d}(\lambda, \lambda_{d,0}, \sigma_{th,0}^2) \sum_{j \in A} H_j(\lambda) d\lambda \\
&+ \tilde{\sigma}_{th}^2(t) I_0 \int_{-\infty}^{+\infty} \frac{\partial G}{\partial \sigma_{th}^2}(\lambda, \lambda_{d,0}, \sigma_{th,0}^2) \sum_{j \in A} H_j(\lambda) d\lambda \\
&+ \sum_{j \in A} X_j(t). \tag{6}
\end{aligned}$$

Likewise $s_B(t)$ is defined as the sum of signals in set B .

By defining the units of H_j in such a way that s_j becomes the effective photon counting rate,⁵ each channel contribution to the sum is weighted properly to address different channel sensitivities. The resulting noise term is also characterized by the Poisson distribution.

We define the normalized fluctuating part of s_A as $\hat{s}_A(t) \equiv s_A(t)/s_{A,0} - 1$ where $s_{A,0}$ is the time average of s_A . We assume that over the interval of the time average, the underlying wave is stationary and it is long enough to make the noise terms negligible. Under these conditions,

$$\hat{s}_A(t) = \frac{\tilde{I}(t)}{I_0} + k_A \tilde{\lambda}_d(t) + c_{T,A} \tilde{\sigma}_{th}^2(t) + x_A, \tag{7}$$

where

$$\begin{aligned}
k_A &\equiv \frac{1}{F_A} \int_{-\infty}^{+\infty} \frac{\partial G}{\partial \lambda_d} \sum_{j \in A} H_j(\lambda) d\lambda, \\
c_{T,A} &\equiv \frac{1}{F_A} \int_{-\infty}^{+\infty} \frac{\partial G}{\partial \sigma_{th}^2} \sum_{j \in A} H_j(\lambda) d\lambda, \\
x_A &\equiv \frac{1}{I_0 F_A} \sum_{j \in A} X_j(t), \\
F_A &\equiv \int_{-\infty}^{+\infty} G(\lambda, \lambda_{d,0}, \sigma_{th,0}^2) \sum_{j \in A} H_j(\lambda) d\lambda.
\end{aligned} \tag{8}$$

We can calculate k_A and $c_{T,A}$ by fitting the time-averaged emission line shape for set A . We similarly normalize $s_B(t)$ and define $\hat{s}_B(t)$ for set B . Since we can most easily distinguish the ion-scale fluctuations by their frequency, we will cross-correlate the frequency spectra $\hat{s}_{A,f}$ and $\hat{s}_{B,f}$, where

$$\hat{s}_{A,f} \equiv \frac{\tilde{I}_f}{I_0} + k_A \tilde{\lambda}_{d,f} + c_{T,A} \tilde{\sigma}_{th,f}^2 + x_{A,f}, \tag{9}$$

and likewise for set B . The subscript f indicates a frequency Fourier transform using FFT methods. Since taking an ensemble assumes that the data are sampled from a stationary random process, we will assume that k_A , k_B , $c_{T,A}$, and $c_{T,B}$ are uncorrelated with any other quantities defined in Eq. (9).

We now have a method of generating cross spectra $\langle \hat{s}_{A,f}^* \hat{s}_{B,f} \rangle$ for any combination of channels A and B . By having summed multiple channels, we increase the photon counts that lead to a small relative noise of $\hat{s}_{A,f}$ and $\hat{s}_{B,f}$. Furthermore, there is no correlation between $x_{A,f}$ and $x_{B,f}$ since we choose

the sets A and B so that they are disjoint, and we are assuming that there is no noise that is correlated across the channels, e.g., power supply fluctuations on the detectors. Therefore, evaluating cross spectra allows us to reject uncorrelated noise, and the contributions from $x_{A,f}$ and $x_{B,f}$ are eliminated. The sensitivity of $\hat{s}_{A,f}$ to the Doppler shift and thermal broadening fluctuations depends on k_A and $c_{T,A}$, respectively, and can be varied by choosing different channel groupings. For example, when we choose spectral channels for A from the right side of the peak, the red shift in the wavelength will increase s_A as shown in Fig. 1. From Fig. 1 and Eq. (8), we can see that k_A takes a large positive value and the sensitivity of $\hat{s}_{A,f}$ to the Doppler shift will increase.

In general, the cross correlation $\langle \hat{s}_{A,f}^* \hat{s}_{B,f} \rangle$ has nine terms and isolating them by evaluating different groupings is challenging. However, we can select groupings so that $\langle \hat{s}_{A,f}^* \hat{s}_{B,f} \rangle$ is less sensitive to a specific type of fluctuation, e.g., velocity versus temperature. There can also be cases where one fluctuating quantity is negligible compared to the others. For example, when $c_{T,A}$ and $c_{T,B}$ are small, the contributions to $\langle \hat{s}_{A,f}^* \hat{s}_{B,f} \rangle$ from thermal broadening are ignorable.

When the conditions of the measurements and groupings allow neglecting thermal broadening, $\langle \hat{s}_{A,f}^* \hat{s}_{B,f} \rangle$ has the form

$$\begin{aligned}
\langle \hat{s}_{A,f}^* \hat{s}_{B,f} \rangle &\approx \left\langle \frac{|\tilde{I}_f|^2}{I_0^2} \right\rangle + \left\langle |\tilde{\lambda}_{d,f}|^2 \right\rangle \langle k_A \rangle \langle k_B \rangle \\
&+ \left\langle \frac{\tilde{I}_f}{I_0} \tilde{\lambda}_{d,f}^* \right\rangle \langle k_A + k_B \rangle \cos \phi \\
&+ i \left\langle \frac{\tilde{I}_f}{I_0} \tilde{\lambda}_{d,f}^* \right\rangle \langle k_A - k_B \rangle \sin \phi, \tag{10}
\end{aligned}$$

where $\arg(\langle \tilde{I}_f \tilde{\lambda}_{d,f}^* \rangle) = \phi$ is the cross phase between the intensity and Doppler-shift fluctuations. A phasor diagram depicting each of the contributions of the terms on the right-hand side of Eq. (10) is shown in Fig. 2. In this specific case, there are only four terms that compose $\langle \hat{s}_{A,f}^* \hat{s}_{B,f} \rangle$ and isolating them becomes somewhat easier by evaluating four different groupings to which Eq. (10) is applicable.

A key limitation for this analysis method is set by the uncertainties in $\langle \hat{s}_{A,f}^* \hat{s}_{B,f} \rangle$ that depend both on the number

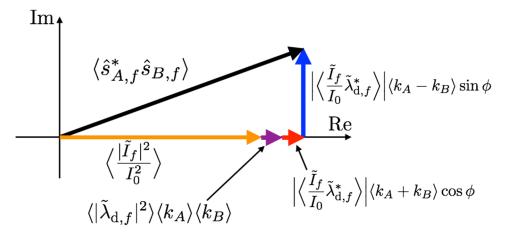


FIG. 2. A phasor diagram that illustrates the components of Eq. (10). The orange and purple arrows measure the power of the intensity and the Doppler shift fluctuations, respectively. The red and blue arrows correspond to the cross-correlated fluctuations between the intensity and Doppler shift fluctuations. The Doppler shift fluctuation that is in-phase with the intensity fluctuation is projected on the red arrow, while the component $\pi/2$ out-of-phase is projected on the blue arrow. Since the Doppler shift is caused by the velocity fluctuation, the red arrow represents the transport of I and the blue arrow represents the circulation of I with no net flux.

of samples in the ensemble and the coherence level of the cross correlation.¹⁴ When the difference in $\langle \hat{s}_{A,f}^* \hat{s}_{B,f} \rangle$ for different groupings cannot be distinguished from uncertainties, the contribution from each term cannot be separated. To keep the uncertainties low, we need to add a sufficient number of channels to achieve a high coherence. This requirement limits the number of useful groupings.

It should also be noted that we are explicitly neglecting any contributions from three-wave interactions. In analogy with gas puff imaging,^{15,16} we are measuring modulated visible emission from the plasma from which we infer the structure of the turbulence. In this analysis, we assume that

$$\left| \left\langle \frac{\tilde{I}_f^*}{I_0} \tilde{\lambda}_{d,f} \right\rangle \right| \gg \left| \left\langle \frac{\tilde{I}_f^*}{I_0} \sum_{f'+f''=f} \frac{\tilde{I}_{f'}}{I_0} \tilde{\lambda}_{d,f''} \right\rangle \right|, \quad (11)$$

where the right-hand side of Eq. (11) corresponds to the three-wave interaction. When Eq. (11) holds, the contribution from $\epsilon_I \epsilon$ in Eq. (A5) is small. Thus, Eq. (10) is still a valid model for the measured cross spectra even when the condition $\epsilon_I \ll 1$ discussed in the Appendix is weakly satisfied.

III. APPLICATIONS OF THE LINEARIZED SPECTRUM CORRELATION ANALYSIS TO RADIAL VELOCITY FLUCTUATION MEASUREMENTS

In this section, we apply LSCA to experimental data for improved-confinement MST reversed field pinch plasmas that have reduced-amplitude tearing instabilities.^{18,19} High frequency density fluctuations (~ 100 kHz) emerge in these plasmas as seen by edge interferometry measurements.¹⁷ We also observe fluctuations with $k_{\perp} \rho_s$ of 0.3 – 0.7 cm^{-1} in C III 464.7 nm emission using the viewing geometry shown in Fig. 3. The line of sight is focused within the edge C III emission shell. Gyrokinetic modeling suggests that these fluctuations are density-gradient-driven trapped electron modes (TEM).^{6,7}

The part of the Doppler-shift fluctuations that are coherent with the intensity fluctuations is determined by making groupings that are insensitive to the thermal broadening fluctuations. An ensemble by collecting time periods showed high

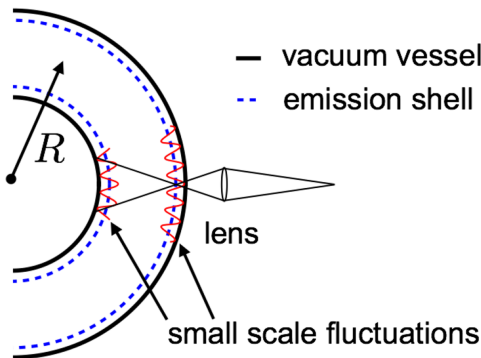


FIG. 3. Schematic of the toroidal cross section of the C III passive spectroscopy measurement. R represents a major radius of torus. The C III emission shell (represented by the dashed blue line) has a significant overlap with the region where the edge density gradient is steepest and where high-frequency fluctuations (depicted as a red sine wave) were previously measured with interferometry.¹⁷

frequency fluctuations from similar discharges and applied LSCA. The measured fluctuations above 100 kHz are dominated by the contribution from the emission shell at the focal point since the fluctuations within the emission shell in the unfocused portion of the line of sight should be averaged out spatially. While fluctuations with a characteristic scale comparable to or larger than the sampling volume are not averaged out, their characteristic frequency should be lower than the frequency of interest and can be separated in the frequency domain. When calculating $s_{A,0}$ and $s_{B,0}$, half of the DC component comes from the unfocused region.

The measured ion temperature in the edge region where the C III emission is localized is $T_I \approx 50$ eV, and the ion thermal speed is $v_{th} \approx 20$ km/s. We estimate the (radial) velocity fluctuation amplitude to be ~ 1 – 2 km/s. Given previous measurements of the ion temperature profile,¹⁸ the ion temperature fluctuation is therefore expected to be $\tilde{T}_I/T_I < 10\%$. Given $\langle \sigma_{th,0} \rangle = 31.4$ pm and $\sigma_H = 45.5$ pm in Eq. (A4), the conditions $\epsilon_d, \epsilon_{th} \ll 1$ described in the Appendix are well satisfied. The analysis discussed in Sec. II is applied to three different channel groupings (I, II, and III) as shown in Fig. 4, and calculated coefficients of fluctuation parameters are shown in Table I using a single Gaussian for G .

The channel distribution of grouping I shown in Fig. 4(a) is symmetric about the emission peak for each set and minimizes the contributions from the Doppler shift and thermal broadening fluctuations. From Table I, we see that if the velocity fluctuation spectrum is on the order of the thermal speed ($\tilde{v}_{r,f}/v_{th,0} = \tilde{\lambda}_{d,f}/\sigma_{th,0}$), their contribution to $\hat{s}_{A,f}$ and $\hat{s}_{B,f}$ would be less than one percent. The plasma has a modest ion temperature gradient compared with that of electron density or C III impurity density. Therefore, $|\tilde{I}_f/I_0| \gtrsim |\sigma_{th,f}^2/\sigma_{th,0}^2|$ is a reasonable assumption implying that temperature fluctuations would also contribute at most at the percent level. These are rather extreme constraints and so we expect the contributions from the velocity and temperature fluctuations in grouping I to be much smaller than 1%. The resulting cross spectrum in Fig. 4(d) has only a real component and a strong coherency that peaks in the 100–200 kHz range. The lack of an imaginary component is consistent with the assumption that the contributions from velocity and temperature fluctuations are negligible. Therefore we interpret the cross spectrum for grouping I as the orange arrow shown Fig. 2, where

$$\langle \hat{s}_{A,f}^* \hat{s}_{B,f} \rangle_I \approx \left\langle \frac{|\tilde{I}_f|^2}{I_0^2} \right\rangle. \quad (12)$$

TABLE I. Ensemble averaged coefficients of small fluctuating parameters defined in Eq. (8). The ensemble average of thermal broadening was used to make the coefficients dimensionless for comparison.

Grouping	I	II	III
$\langle k_A \rangle \sqrt{\langle \sigma_{th,0}^2 \rangle}$	5.65×10^{-4}	-6.18×10^{-1}	-8.92×10^{-1}
$\langle k_B \rangle \sqrt{\langle \sigma_{th,0}^2 \rangle}$	-9.12×10^{-3}	4.67×10^{-1}	8.85×10^{-1}
$\langle k_A - k_B \rangle \sqrt{\langle \sigma_{th,0}^2 \rangle}$	9.72×10^{-3}	-1.09×10^0	-1.78×10^0
$\langle c_{T,A} \rangle \langle \sigma_{th,0}^2 \rangle$	-3.41×10^{-2}	-4.57×10^{-3}	1.54×10^{-1}
$\langle c_{T,B} \rangle \langle \sigma_{th,0}^2 \rangle$	-1.08×10^{-2}	-3.47×10^{-2}	2.07×10^{-1}

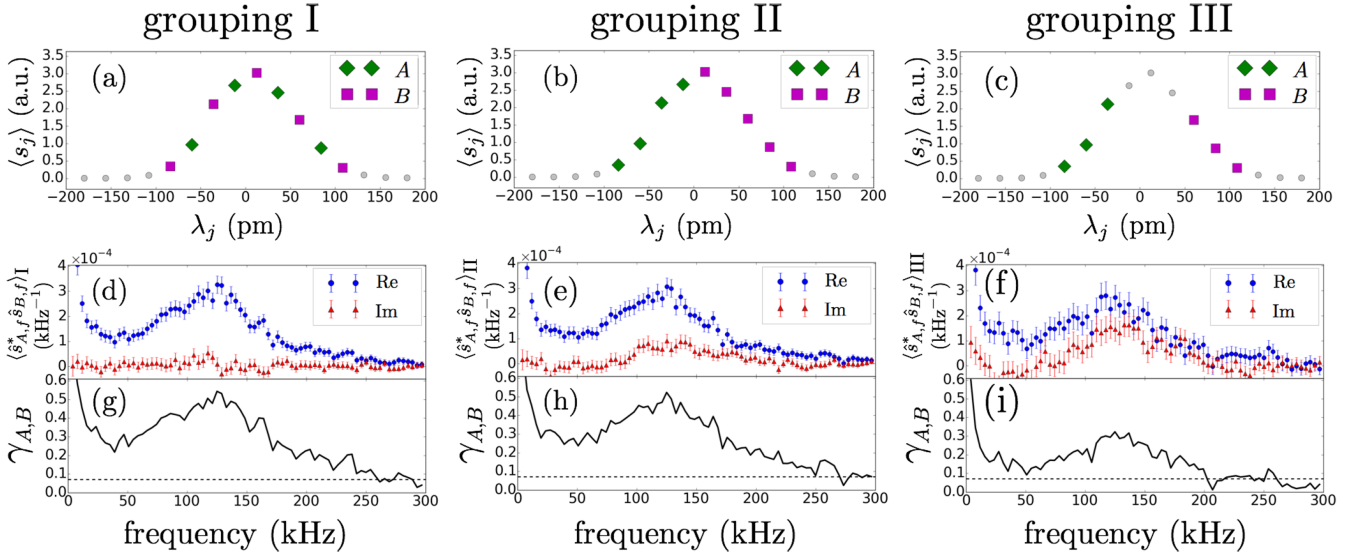


FIG. 4. Grouping of spectral channels [(a)-(c)], cross spectra [(d)-(f)], and coherence [(g)-(i)] between $\hat{s}_{A,f}$ and $\hat{s}_{B,f}$ for three different groupings. The gray dashed lines for coherence plots are the significance levels. λ_j is the wavelength of spectral channel j with respect to 464.7 nm.

The integrated cross spectrum yields an rms value of $\tilde{I}/I_0 = 0.21$ for the whole spectrum and 0.14 for the 100–200 kHz frequency range. Although I depends not only on the C III density fluctuations but also on the electron density and on the electron temperature fluctuations, the fluctuation power spectrum for I is similar to that of the electron density fluctuations measured by interferometry measurements suggesting that the fluctuations of I capture the structure of the turbulence, implying Eq. (11) is a reasonable assumption.

In grouping II in Fig. 4(b), the channels for set A are taken from the left side of the emission peak, while the channels for set B are from the right side. This grouping increases the magnitude of $\langle k_A - k_B \rangle$ in Table I two orders of magnitude and makes it explicitly negative, while the coefficients of the thermal broadening terms remain small. Now if the velocity fluctuations are a significant fraction of the ion thermal speed, they contribute to the normalized signal spectrum at the same order as the intensity fluctuations. We use Eq. (10) to interpret the cross spectrum for grouping II as

$$\begin{aligned} \langle \hat{s}_{A,f}^* \hat{s}_{B,f} \rangle_{\text{II}} &\approx \left\langle \frac{|\tilde{I}_f|^2}{I_0^2} \right\rangle + \langle |\tilde{\lambda}_{d,f}|^2 \rangle \langle k_A \rangle_{\text{II}} \langle k_B \rangle_{\text{II}} \\ &+ \left\langle \frac{\tilde{I}_f \tilde{\lambda}_{d,f}^*}{I_0} \right\rangle \langle k_A + k_B \rangle_{\text{II}} \cos \phi \\ &+ i \left\langle \frac{\tilde{I}_f \tilde{\lambda}_{d,f}^*}{I_0} \right\rangle \langle k_A - k_B \rangle_{\text{II}} \sin \phi. \end{aligned} \quad (13)$$

We find that the real part of the cross spectrum for grouping II in Fig. 4(e) is very similar to that of grouping I with a similar strong coherency, but the imaginary part is now non-negligible implying a significant contribution from the velocity fluctuations in the fourth term of Eq. (13) depicted as the blue arrow in the phasor diagram in Fig. 2.

For linear electrostatic fluctuations, radial velocity fluctuations are coherent with and proportional to density fluctuations when the electron response is adiabatic. They arise

from $\mathbf{E} \times \mathbf{B}$ flows that are $\pi/2$ out-of-phase with the density fluctuations. If the observed intensity fluctuations arise from linear electrostatic fluctuations, then these circulating flows will appear as Doppler-shift fluctuations in the imaginary part of the cross spectrum in grouping II with

$$\begin{aligned} \frac{\text{Im} \langle \hat{s}_{A,f}^* \hat{s}_{B,f} \rangle_{\text{II}}}{\sqrt{\text{Re} \langle \hat{s}_{A,f}^* \hat{s}_{B,f} \rangle_{\text{I}}}} &\approx \frac{\left\langle \frac{\tilde{I}_f \tilde{\lambda}_{d,f}^*}{I_0} \right\rangle}{\sqrt{\left\langle \frac{|\tilde{I}_f|^2}{I_0^2} \right\rangle}} \langle k_A - k_B \rangle_{\text{II}} \sin \phi \\ &\approx |\tilde{\lambda}_{d,f}| \langle k_A - k_B \rangle_{\text{II}} \sin \phi. \end{aligned} \quad (14)$$

Using Eq. (14) and the value for $\langle k_A - k_B \rangle_{\text{II}}$ shown in Table I, the calculated corresponding velocity fluctuation spectrum is shown in Fig. 5(b). The intensity spectrum calculated from $\langle \hat{s}_{A,f}^* \hat{s}_{B,f} \rangle_{\text{I}}$ is also shown in Fig. 5(a) for comparison. The peak near 130 kHz seen in Fig. 5 is distinct from tearing modes that peak below 30 kHz.²⁰ Integrating the velocity fluctuation spectrum gives an rms-amplitude of 1 km/s which is a lower bound on the total radial velocity fluctuation amplitude.

For grouping III in Fig. 4(c), the magnitude of $\langle k_A - k_B \rangle_{\text{III}}$ is larger than $\langle k_A - k_B \rangle_{\text{II}}$. The imaginary part of $\langle \hat{s}_{A,f}^* \hat{s}_{B,f} \rangle_{\text{III}}$ shown in Fig. 4(f) becomes comparable to the real part, but the coherence level is noticeably reduced in Fig. 4(i) since a

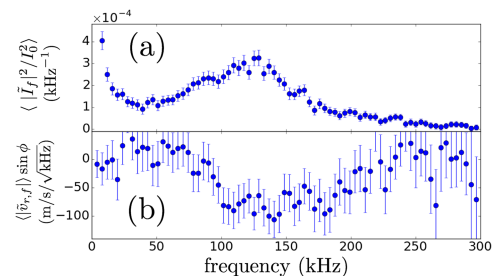


FIG. 5. C III emission intensity fluctuation spectrum (a) and radial velocity fluctuation spectrum (b) for a 380 kA improved-confinement plasma.

smaller number of channels are added in grouping III. From Table I, we also see that thermal broadening fluctuations could contribute to $\langle \hat{s}_{A,f}^* \hat{s}_{B,f} \rangle_{\text{III}}$ and Eq. (10) may not be applicable. Considering the size of the error bars, it is difficult to isolate thermal broadening fluctuations using grouping III. Other groupings that have larger magnitudes for $c_{T,A}$ and $c_{T,B}$ and smaller magnitudes of k_A and k_B show no sign of thermal broadening fluctuations. Unfortunately, there are insufficient data to quantify other quantities such as the in-phase part of the radial velocity and temperature fluctuations. If we collect more photons from the emission line or accumulate more statistics, we can reduce the uncertainties and may be able to measure other quantities of interest with precision.

IV. COMPARISON BETWEEN LINEARIZED SPECTRUM CORRELATION ANALYSIS AND MOMENT ANALYSIS USING SYNTHESIZED DATA

In order to compare the resolution available through LSCA as opposed to MA, we run Monte Carlo simulations and apply both analysis techniques to synthesized data created from Eq. (3). The parameters used in the simulations are shown in Table II. Poisson(N) returns a pseudorandom sample drawn from the Poisson distribution function with the expectation value of N . To measure velocity fluctuations using LSCA, a cross spectrum needs to be divided by the square root of the intensity fluctuation power as shown in Eq. (14). The factor Poisson(50) adds coherent intensity fluctuations over all frequencies and allows us to measure the frequency components of velocity fluctuation at all frequencies. The noise term X_j is accounted for by sampling from a Poisson distribution. After calculating the expected photon counts for each time point, we determine s_j by drawing a pseudorandom sample from the Poisson distribution with an expectation value of the expected photon count. An example of synthesized data points is shown in Fig. 6(a). We can see that the uncertainties introduced by the Poisson noise lead to a significant deviation from the true line shape. Line shape fitting techniques become sensitive to the initial values of fit parameters and difficult to implement. Figure 6(b) shows the time average of the synthesized data over the FFT time window. The Poisson noise has been reduced to an acceptable level, and k_A and $c_{T,A}$ in Eq. (9) can be measured with precision.

TABLE II. Simulation parameters were chosen so that they give results comparable to the spectra shown in Fig. 5 with a sharp peak at $f = 100$ kHz. The average photon counting rate is defined for the sum of all channels.

Quantity	Value
$I(t)$	$\propto \text{Poisson}(50)(1 + 0.06 \cos(2\pi ft))$
$\tilde{\lambda}_d(t)$	$0.62 \cos(2\pi ft - \pi/2)$ (pm)
H_j	Similar to Fig. 6 in Ref. 3
G	Single Gaussian for C III 464.7 nm emission line $T_1 = 51$ eV
Average photon count rate	25 (photons/ μs)
Sampling rate	1 MHz
Time points	200 000
Hamming window width	256 μs

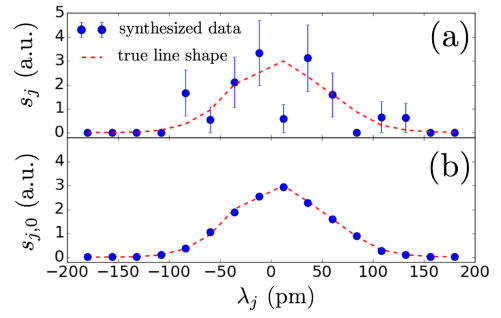


FIG. 6. Example of synthesized data points (a) and data points averaged over 256 μs (b). The error bars are estimated assuming the Poisson statistics. The data points without an error bar have zero photon counts. The wavelength spacing between adjacent spectral channels is 24 pm.

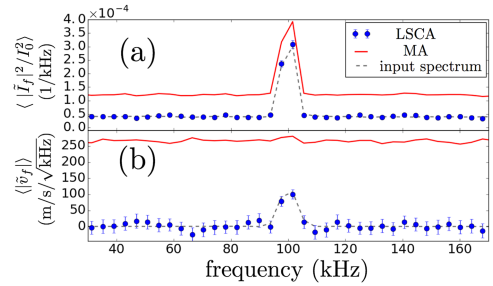


FIG. 7. Intensity (a) and velocity (b) spectra. The velocity spectrum was calculated from the Doppler shift.

The simulation results are shown in Fig. 7. We use Eq. (10) for all groupings in LSCA since there are no temperature fluctuations, and the contribution of the factor Poisson(50) to $\tilde{I}(t)/I_0$ which is not coherent with $\tilde{\lambda}_d$ is small compared with that of $\cos(2\pi ft)$ at 100 kHz. We can see that LSCA reproduces the input spectra for intensity and velocity fluctuations. On the other hand, MA overestimates the intensity power spectral density and shows no structure in the velocity fluctuation spectrum at 100 kHz. By plugging the parameters of this simulation, $f_{\text{Nyquist}} = 500$ kHz and $\sum_j n_j = 25$ into Eq. (1), the Poisson noise contribution to the intensity power spectral density is calculated to be $P_{f,\text{noise}} = 0.8 \times 10^{-4} \text{ kHz}^{-1}$ which is consistent with the difference between the MA spectrum and the input spectrum in Fig. 7(a). As for the velocity fluctuation spectra, the signal level is below the noise floor and cannot be resolved in MA. In contrast to MA, the noise floors are reduced in LSCA. In the limit where the number of samples in the ensemble goes to infinity, LSCA is able to reproduce the input spectra completely.

V. SUMMARY

A new method which we call linearized spectrum correlation analysis (LSCA) for passive and charge-exchange impurity emission and an application of it are presented. LSCA rejects uncorrelated noise by using a combination of ensemble averaging and cross correlation to improve the resolution of line emission measurements as the sample size increases. Using LSCA, the fast radial impurity velocity fluctuations (100–200 kHz) associated with ion-scale micro-instabilities

are detected. When LSCA and MA are applied to the synthesized data, LSCA provides better resolutions than MA.

SUPPLEMENTARY MATERIAL

See [supplementary material](#) for the digital format of the data shown in this paper.

ACKNOWLEDGMENTS

This work is supported by the U.S. Department of Energy, Office of Science, and Office of Fusion Energy Sciences under Award No. DE-FC02-05ER54814.

APPENDIX: LINEARIZATION CRITERIA

Here we summarize the criteria for linearizing spectral channel outputs. To simplify the discussion, we assume that the normalized emission line and instrumental transfer function are Gaussian,

$$G(\lambda, \lambda_d, \sigma_{th}^2) = \frac{1}{\sqrt{2\pi\sigma_{th}^2}} \exp\left[-\frac{(\lambda - \lambda_d)^2}{2\sigma_{th}^2}\right], \quad (A1)$$

$$H_j(\lambda) = \frac{1}{\sqrt{2\pi\sigma_H^2}} \exp\left[-\frac{(\lambda - \lambda_j)^2}{2\sigma_H^2}\right], \quad (A2)$$

where σ_H^2 quantifies the spectral resolution, and λ_j is the central location of a spectral channel measured with respect to the unshifted emission line wavelength λ_0 . Using Eq. (3), the output of the spectral channel j is

$$s_j(I, \lambda_d, \sigma_{th}^2) = \frac{I}{\sqrt{2\pi(\sigma_{th}^2 + \sigma_H^2)}} \exp\left[-\frac{(\lambda_j - \lambda_d)^2}{2(\sigma_{th}^2 + \sigma_H^2)}\right]. \quad (A3)$$

Here, the noise term is neglected. We introduce dimensionless parameters based on the assumptions of Eq. (5),

$$\begin{aligned} \epsilon_I &\equiv \frac{\tilde{I}}{I_0}, & \epsilon_d &\equiv \frac{\tilde{\lambda}_d}{\sqrt{\sigma_{th,0}^2 + \sigma_H^2}}, \\ \epsilon_{th} &\equiv \frac{\tilde{\sigma}_{th}^2}{\sigma_{th,0}^2 + \sigma_H^2}, & \delta_j &\equiv \frac{\lambda_j - \lambda_{d,0}}{\sqrt{\sigma_{th,0}^2 + \sigma_H^2}}. \end{aligned} \quad (A4)$$

When $\epsilon_d, \epsilon_{th} \ll 1$, δ_j needs to be on the order of unity in order for s_j to have a non-negligible amplitude compared with spectral channel outputs near the emission peak. Therefore, when the conditions $\epsilon_d, \epsilon_{th} \ll 1$ are satisfied, we can expand s_j in terms of ϵ_d and ϵ_{th} as follows:

$$\begin{aligned} s_j &= \frac{I_0 e^{-\frac{1}{2}\delta_j^2}}{\sqrt{2\pi(\sigma_{th,0}^2 + \sigma_H^2)}} \\ &\times \left[1 + \epsilon_I + \delta_j \epsilon_d - \frac{1 - \delta_j^2}{2} \epsilon_{th} + \mathcal{O}(\epsilon_I \epsilon, \epsilon^2) \right], \end{aligned} \quad (A5)$$

where $\epsilon = \epsilon_d, \epsilon_{th}$.

In general, H_j is not necessarily Gaussian, but it is likely centrally peaked with some characteristic width that can be estimated by σ_H . With this approximation, if $\epsilon_d, \epsilon_{th} \ll 1$, that is, if the velocity fluctuations are much smaller than the ion thermal speed and temperature fluctuations are much smaller than the mean temperature, then Eq. (3) can be linearized according to Eq. (4).

- ¹I. U. Uzun-Kaymak, R. J. Fonck, and G. R. McKee, *Rev. Sci. Instrum.* **83**, 10D526 (2012).
- ²D. D. Truong, R. J. Fonck, and G. R. McKee, *Rev. Sci. Instrum.* **87**, 11E551 (2016).
- ³D. Craig, D. J. Den Hartog, D. A. Ennis, S. Gangadhara, and D. Holly, *Rev. Sci. Instrum.* **78**, 013103 (2007).
- ⁴R. Dexter, D. Kerst, T. Lovell, S. Prager, and J. Sprott, *Fusion Sci. Technol.* **19**, 131 (1991).
- ⁵T. Nishizawa, M. D. Nornberg, D. J. Den Hartog, and D. Craig, *Rev. Sci. Instrum.* **87**, 11E530 (2016).
- ⁶D. Carmody, M. J. Pueschel, and P. W. Terry, *Phys. Plasmas* **20**, 052110 (2013).
- ⁷D. Carmody, M. J. Pueschel, J. K. Anderson, and P. W. Terry, *Phys. Plasmas* **22**, 012504 (2015).
- ⁸H. Evensen, R. Fonck, S. Paul, G. Rewoldt, S. Scott, W. Tang, and M. Zarnstorff, *Nucl. Fusion* **38**, 237 (1998).
- ⁹D. J. Den Hartog, A. F. Almagri, S. C. Prager, and R. J. Fonck, *Rev. Sci. Instrum.* **66**, 444 (1995).
- ¹⁰M. Podestà and R. E. Bell, *Rev. Sci. Instrum.* **83**, 033503 (2012).
- ¹¹S. Gangadhara, D. Craig, D. A. Ennis, and D. J. Den Hartog, *Rev. Sci. Instrum.* **77**, 10F109 (2006).
- ¹²G. Cima, R. V. Bravenec, A. J. Wootton, T. D. Rempel, R. F. Gandy, C. Watts, and M. Kwon, *Phys. Plasmas* **2**, 720 (1995).
- ¹³S. Sattler and H. J. Hartfuss, *Phys. Rev. Lett.* **72**, 653 (1994).
- ¹⁴J. S. Bendat and A. G. Piersol, *Random Data: Analysis and Measurement Procedures*, 4th ed. (John Wiley & Sons, 1971).
- ¹⁵R. J. Maqueda, G. A. Wurden, D. P. Stotler, S. J. Zweben, B. LaBombard, J. L. Terry, J. L. Lowrance, V. J. Mastrocola, G. F. Renda, D. A. D'Ippolito, J. R. Myra, and N. Nishino, *Rev. Sci. Instrum.* **74**, 2020 (2003).
- ¹⁶I. Cziegler, P. H. Diamond, N. Fedorczak, P. Manz, G. R. Tynan, M. Xu, R. M. Churchill, A. E. Hubbard, B. Lipschultz, J. M. Sierchio, J. L. Terry, and C. Theiler, *Phys. Plasmas* **20**, 055904 (2013).
- ¹⁷J. Sarff, A. Almagri, J. Anderson, M. Borchardt, W. Cappechi, D. Carmody, K. Caspary, B. Chapman, D. Den Hartog, J. Duff, S. Eilerman, A. Falkowski, C. Forest, M. Galante, J. Goetz, D. Holly, J. Koliner, S. Kumar, J. Lee, D. Liu, K. McCollam, M. McGarry, V. Mirnov, L. Morton, S. Munaretto, M. Nornberg, P. Nonn, S. Oliva, E. Parke, M. Pueschel, J. Reusch, J. Sauppe, A. Seltzman, C. Sovinec, D. Stone, D. Theucks, M. Thomas, J. Triana, P. Terry, J. Waksman, G. Whelan, D. Brower, W. Ding, L. Lin, D. Demers, P. Fimognari, J. Titus, F. Auriemma, S. Cappello, P. Franz, P. Innocente, R. Lorenzini, E. Martinez, B. Momo, P. Piovesan, M. Puiatti, M. Spolaore, D. Terranova, P. Zanca, V. Davydenko, P. Deichuli, A. Ivanov, S. Polosatkin, N. Stupishin, D. Spong, D. Craig, H. Stephens, R. Harvey, M. Cianciosa, J. Hanson, B. Breizman, M. Li, and L. Zheng, *Nucl. Fusion* **55**, 104006 (2015).
- ¹⁸B. E. Chapman, A. F. Almagri, J. K. Anderson, T. M. Biewer, P. K. Chattopadhyay, C.-S. Chiang, D. Craig, D. J. Den Hartog, G. Fiksel, C. B. Forest, A. K. Hansen, D. Holly, N. E. Lanier, R. O'Connell, S. C. Prager, J. C. Reardon, J. S. Sarff, M. D. Wyman, D. L. Brower, W. X. Ding, Y. Jiang, S. D. Terry, P. Franz, L. Marrelli, and P. Martin, *Phys. Plasmas* **9**, 2061 (2002).
- ¹⁹J. K. Anderson, J. Adney, A. Almagri, A. Blair, D. L. Brower, M. Cengher, B. E. Chapman, S. Choi, D. Craig, D. R. Demers, D. J. Den Hartog, B. Deng, W. X. Ding, F. Ebrahimi, D. Ennis, G. Fiksel, C. B. Forest, P. Franz, J. Goetz, R. W. Harvey, D. Holly, B. Hudson, M. Kaufman, T. Lovell, L. Marrelli, P. Martin, K. McCollam, V. V. Mirnov, P. Nonn, R. O'Connell, S. Oliva, P. Piovesan, S. C. Prager, I. Predebon, J. S. Sarff, G. Spizzo, V. Svidzinski, M. Thomas, and M. D. Wyman, *Phys. Plasmas* **12**, 056118 (2005).
- ²⁰S. Assadi, S. C. Prager, and K. L. Sidikman, *Phys. Rev. Lett.* **69**, 281 (1992).